

Article

# A Method of Estimating Mutual Inductance and Load Resistance Using Harmonic Components in Wireless Power Transfer System

Dongsheng Yang <sup>1</sup>, Sokhui Won <sup>1,2,†</sup>, Jiangwei Tian <sup>1,\*</sup>, Zixin Cheng <sup>1</sup> and Jongho Kim <sup>2</sup>

<sup>1</sup> School of Information Science and Engineering, Northeastern University, Shenyang 110819, China

<sup>2</sup> Institute of Electronic, State Academy of Sciences, Kwahak-1 Dong, Unjong District, Pyongyang 999093, Korea

\* Correspondence: 1770474@stu.neu.edu.cn; Tel.: +86-1862-432-6316

† These authors contributed equally to this work.

Received: 13 June 2019; Accepted: 13 July 2019; Published: 17 July 2019



**Abstract:** In general, for the WPT (Wireless Power Transfer) system, as the mutual inductance and load resistance are calculated according to the measured data of both the transmitter and receiver, the wireless communication modules are needed to share data. A method for estimating mutual inductance and load resistance without wireless communication is proposed, based on the fundamental and third harmonic components. The circuit is decomposed with respect to the frequencies, by which the mathematic model is established. The fundamental and harmonic components of the output voltage and current of a high-frequency inverter are found by FFT (Fast Fourier Transform). The experimental WPT system with a SiC power MOSFET is designed, and the effectiveness of the proposed method is verified by the simulation and experiment results. Additional hardware and frequency scanning operation are not needed because of the use of the harmonic components.

**Keywords:** wireless power transfer; harmonic frequency; fast fourier transform; mutual inductance and load resistance

## 1. Introduction

Researchers are interested in the Wireless Power Transfer (WPT) system currently due to the merit of being able to transfer electric energy without a transmission cable, and many research teams have been studying the WPT system. Recently, WPT technology has been widely used to charge small-power electronic devices such as electric brushing machines and mobile phones [1,2] and high-power products for charging electric vehicles [3,4]. The WPT system is also used in biomedical machine applications [5–7], and the trouble caused by having to perform the surgery for replacing the battery is avoided. In addition to wireless charging, it is also used as wireless power supply sources for TVs [8], electronic shelf labels [9], wearable electronic products [10–12], and various card powers [13]. The WPT system is also used for mobile aluminum furnaces [14] and kitchen appliances [15,16], and it is able to transfer the electric power to the load without using any cable and the receiver's rectifier.

According to the transmission medium, the WPT system is mainly categorized into four types: electromagnetic induction [17–19], magnetic resonance coupling [20,21], electric field coupling [22,23], and electromagnetic wave [24–26]. Besides, ultrasonic [27] and lasers [28] are also used. Among those WPT types, the magnetic coupling resonance method is the most commonly used, and research on this method is the hottest because it has the advantage of being able to transmit the electricity at a long distance.

Generally, the Magnetic Resonance Coupling Wireless Power Transfer (MRC-WPT) system consists of three parts, namely a high-frequency power supply, a coil set (transmitting and receiving coil; some systems may have more than one intermediate coil in the coil set), and a receiver circuit. The coupling coefficient (or mutual inductance) between the coils and the load resistance are directly related to the performance of the system (for example, efficiency, transfer power, etc.) [29–31].

The measured data of the load voltage and/or current of the receiver are transferred to the transmitter through wireless communication, and these data take part in realizing the constant current, constant voltage, or constant power of the load.

In [32,33], the methods for keeping the constant voltage of the load were represented using the communication module. In [34], the method for maintaining the constant voltage and the current of the load was realized using the communication module. It was implied that the relative position between the transmitter and the receiver moved infrequently, and the internal resistance of the battery was very slowly changed when charging the battery of an electric vehicle, then the concept of the weak communication was defined. In spite of the communication environment being unstable, the load resistance and mutual inductance could be derived, but the communication function was not completely removed from the system. Due to the use of the wireless communication module, the power consumption may be increased, and the normal communication function cannot be performed in some severe situations. It is more unacceptable that if only one of the communication modules among the transmitter and the receiver is damaged, the whole WPT system cannot be operated. In [35], a method in which power and data were transferred at the same time through only one coil was proposed.

If the load voltage and/or current can be estimated without any measured data of the receiver, the difficulties mentioned above do not need to be considered; while, if the inductance and capacitance of the receiver ( $L_2$ ,  $C_2$ ), resonance frequency  $\omega$ , and the circuit topology are given, the voltage, current, and power of the receiver can be deduced with the transmitter current, load resistance, and mutual inductance. In other words, as long as the load resistance and the mutual inductance are given, the WPT system does not need the communication function, as the measured data of the receiver are not present for estimating the load voltage and/or current. If the mutual inductance and load resistance can be derived only with the measured data of the transmitter, the load voltage and/or current can be estimated without the communication, and the trouble due to the communication can be avoided.

The method to estimate the mutual inductance and/or load resistance without the communication function have been researched.

In [36], a method for deriving mutual inductance without the communication function was described, in which the value of load resistance must be given before. In [37], a method for deriving the mutual inductance only with the measurement data of the transmitter or receiver was proposed. Similar to [36], the load resistance and mutual inductance cannot be derived at the same time. A method for simultaneously measuring mutual inductance and load resistance of the S-S (Series-Series) topological WPT was proposed in [38]. The frequency scanning was performed near the resonant frequency, and then, the mutual inductance and load resistance were solved from these frequency equations. Moreover, a normal function generator and a linear power amplifier were utilized for experimentally verifying the validity of the proposed method. In [39], a method for simultaneously measuring mutual inductance and load resistance of the S-S topology WPT was proposed, in which two action modes were realized by substituting the compensation capacities, and then, mutual inductance and load resistance were solved from two sets of equations.

The WPT system mentioned in [40] utilized the S-P (Series-Parallel) topology. Only the data of the transmitter were measured, and these data were decomposed into real and imaginary parts. Based on the two equations, the mutual inductance was obtained. Unfortunately in the S-P topology, the optimal frequency is also changed with the variations of the mutual inductance and load resistance. In [41], a method for deriving load resistance and mutual inductance of S-P and P-P (Parallel-Parallel) topological WPT systems was presented, in which the same problem had to be solved as appeared in

[40]. In [42], a method of increasing the operating frequency and reducing the volume was developed by using harmonic currents.

In the common WPT system, it must have a high-frequency inverter. In order to avoid the power loss of the switching elements, the driving signals are close to the rectangle waveform, which means that there are many harmonics. Despite the fact that the series LC resonant circuit of the S-S topology WPT can be considered as a filter circuit, some harmonic components can be included in the output current. In this paper, the method of simultaneously estimating the mutual inductance and the load resistance using the harmonic components of the transmitter output voltage and current is proposed for the case where the switch driving frequency is constant and there is no communication function for data transfer from a receiver to a transmitter. The experimental WPT system with the SiC MOSFET switch elements is set up, and the effectiveness of the method is verified by the simulation and the experiment.

## 2. Theoretical Analysis

In this section, the relationship between the mutual inductance and the load resistance and the voltage and current of the transmitter and receiver in a WPT system with the communication function is described. Then, the method of simultaneously estimating the mutual inductance and the load resistance with the harmonic components is proposed. This paper is intended to deal with a WPT system without any shielding structures including ferrite cores, and therefore, it is not necessary to consider the nonlinearity of the core with respect to the operating frequency. Consequently, when the energy is exchanged through the mutual inductance, the nonlinear changes of the amplitude and the phase would not happen. The WPT system, in general, is operated in a variable situation, such as a change in transmission distance and/or a change in load resistance. In order to improve the performance of the system, it is necessary to estimate the mutual inductance and the load resistance accurately. Most of the automotive vehicle wireless charging systems on the market today have two coils (transmitter and receiver), and the two-coil topology system is considered here. During the design step, the model and target performance parameters were already given, and the geometrical shape of the transmitter and receiver coils were also designed by the designer. Based on these mentioned concepts above and the structural characteristics of the already used WPT system, several conditions should be assumed as follows:

1. The geometric parameters of the transmitter and the receiver coils are not changed; hence, the circuit parameters are also unchanged and are given as constants.
2. The resonant compensated capacitance values of the transmitter and receiver are given as constants.
3. The resonant frequency of the transmitter and receiver is equal to the frequency of the high-frequency inverter.

In addition to the fact that the calculation process is simple, the S-S resonance circuit has many other other advantages, so it is most commonly used in practical applications; consequently, this topology of the MRC-WPT system is considered here.

### 2.1. The Mutual Inductance and the Load Resistance in the MRC-WPT System with the Wireless Communication Function

The description of how to get the mutual inductance and load resistance simultaneously in the traditional MRC-WPT system with the wireless communication function is detailed as follows. Such MCR-WPT systems have a wireless communication function, a voltage, and/or a current sensor in both the transmitter and receiver side. Figure 1 is the equivalent circuit of the S-S topology MRC-WPT system.

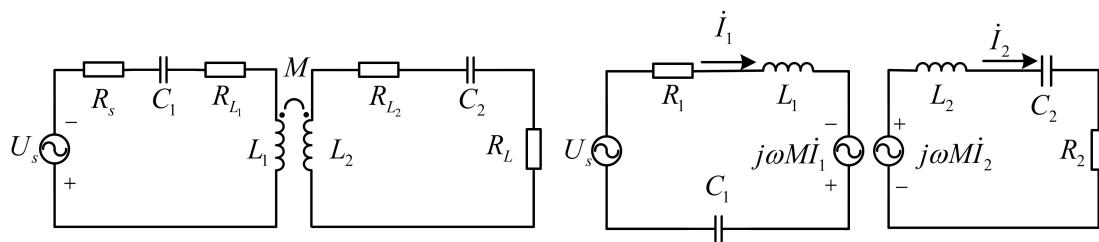


**Figure 1.** Equivalent circuit of the Series-Series (S-S) topology Magnetic Resonance Coupling Wireless Power Transfer (MRC-WPT) system.

Since the transmitter and the receiver are S-S type topologies, the theory of the mutual inductance circuit and Kirchhoff's voltage law were applied to these circuits, and the results are shown as follows.

$$\begin{cases} \dot{U}_s = Z_1 \dot{I}_1 - j\omega M \dot{I}_2 \\ 0 = j\omega M \dot{I}_1 - Z_2 \dot{I}_2 \end{cases} \quad (1)$$

where:

$$\begin{cases} Z_1 = R_1 + j\omega L_1 + \frac{1}{j\omega C_1} \\ Z_2 = R_2 + j\omega L_2 + \frac{1}{j\omega C_2} \end{cases} \quad (2)$$

In Figure 1,  $U_s$  is the high-frequency power supply,  $R_{L1}$  and  $R_{L2}$  are the resistance of the transmitter and receiver coil, respectively,  $R_s$  and  $R_L$  are the protection resistance and the load resistance, respectively,  $L_1$  and  $L_2$  are the self-inductance of the transmitter and receiver coil, respectively,  $R_1 (=R_s + R_{L1})$  is the sum of the over-current protection resistance and the stray resistance of the transmitter circuit, and  $R_2 (=R_L + R_{L2})$  is the sum of the load resistance and the stray resistance of the receiver circuit.  $C_1$  and  $C_2$  are the transmitter and the receiver resonance capacitance.  $I_1$  and  $I_2$  are the currents of the transmitter and the receiver, respectively, and  $M$  is the mutual inductance between two coils. The mutual inductance  $M$  and the load resistance  $R_2$  can be solved by Equations (1) and (2).

$$\begin{cases} M = j \frac{\dot{U}_s - Z_1 \dot{I}_1}{\omega \dot{I}_2} \\ R_2 = Z_2 - j(\omega L_2 - \frac{1}{j\omega C_2}) = \frac{\dot{I}_1}{\dot{I}_2} (\dot{U}_s - Z_1 \dot{I}_1) - j(\omega L_2 - \frac{1}{j\omega C_2}) \end{cases} \quad (3)$$

In Equation (3), the resonant frequencies of the two circuit are equal, and the frequency of the high-frequency driving source is also equal to this frequency. Therefore, the imaginary parts of the equivalent circuit impedances are zero on both sides, and the impedances become the resistances. It is implied that if both sides of the circuit are designed to be in a resonant state, it is not necessary to consider the phase, and only the magnitude of the voltage and current are taken into account. Therefore, Equation (3) is reduced to Equation (4).

$$\begin{cases} M = \frac{(U_s - R_1 I_1)}{\omega I_2} \\ R_2 = \frac{I_1}{I_2} \frac{(U_s - R_1 I_1)}{I_2} \end{cases} \quad (4)$$

From Equation (3), it can be realized that if the current and voltage of the transmitter and the current of the receiver are known, the mutual inductance and the load resistance can be estimated. Because the receiver is away from the transmitter and, moreover, there is no connection wire between two circuits, it is impossible to exchange the measured data. Therefore, some WPT systems may have wireless communication modules, and the measured data are shared between the transmitter and the receiver through this communication; based on these data, the mutual inductance and the load resistance can be represented by Equation (3). Both sides of the circuit are commonly in the resonant state, so the simplified Equation (4) is more practical and commonly used. It is emphasized here that the waveform of the high-frequency power supply is considered to be a pure sine wave.

2.2. Estimating the Mutual Inductance and the Load Resistance on the Transmitter without the Communication Function

Figure 2a is the proposed WPT system equivalent circuit; very similar to Figure 1, the structure is the same, and the only difference is the driving source compared with Figure 1. In Figure 1, the driving source is the sinusoidal voltage source, but in Figure 2a, it is the rectangle voltage source. In Figure 2b, an equivalent circuit decomposed with respect to high order harmonics is shown. Figure 2c is an equivalent circuit simplified by the reflection impedance method.  $Z_s$  is the equivalent impedance of the transmitter, which is equal to the equivalent impedance of the transmitter, and  $Z_r$  is the reflection impedance based on mutual inductance theory,  $Z_r = \frac{(\omega M)^2}{Z_2}$ .

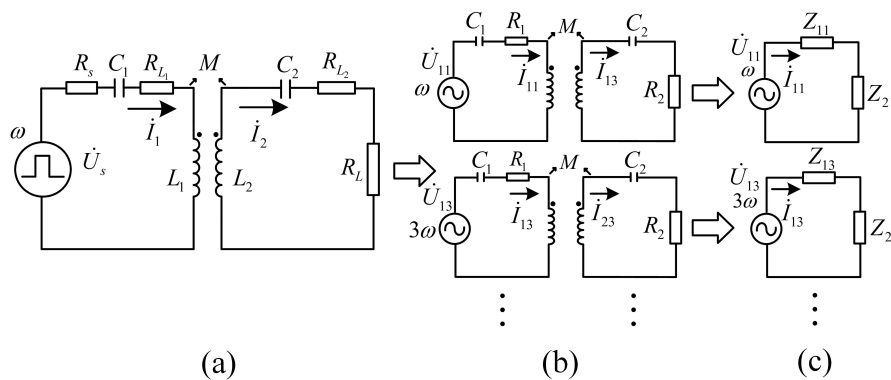


Figure 2. Decomposition diagram for the circuit with the harmonics components. (a) Equivalent circuit with rectangle power source; (b) decomposed circuit; (c) circuit represented using reflection resistance.

In Figure 2a,  $U_s$  is a high-frequency rectangle voltage source. If the frequency of the rectangle voltage source is given and all of the elements in the system is independent of the frequency variation, the element parameters of each circuit, which are decomposed with respect to several harmonic frequencies, are the same. In other words, as shown in Figure 2b, because the mutual inductance is also independent of the frequency variation, all decomposed circuits have the same structure, except the frequency of the sinusoidal driving source.

In the harmonic components that are contained in the output voltage and current of the transmitter circuit, the third harmonic makes up most of it; therefore, this order harmonics component was used here. Although the higher frequency components such as 5, 7, and so on, can be used in theory, the higher the number of harmonics, the smaller its content, and the magnitude of these quantities may be smaller than the measurement error, so it will not be considered. From the equivalent circuit of Figure 2c, Equation (5) is followed for the fundamental and the third harmonic components.  $Z_{11}$  and  $Z_{13}$  are the impedance of the transmitter for the frequencies of the fundamental and the third harmonic circuits, respectively.  $Z_{21}$  and  $Z_{23}$  are the reflection impedance of the receiver for the frequencies of the fundamental and the third harmonic circuit, respectively.

$$\begin{cases} \dot{U}_{11} = i_{11}(Z_{11} + \frac{\omega^2 M^2}{Z_{21}}) \\ \dot{U}_{13} = i_{13}(Z_{13} + \frac{\omega_3^2 M^2}{Z_{23}}) \end{cases} \quad (5)$$

where:

$$\begin{cases} Z_{11} = R_1 + j\omega L_1 + \frac{1}{j\omega C_1} \\ Z_{21} = R_2 + j\omega L_2 + \frac{1}{j\omega C_2} \\ Z_{13} = R_1 + j\omega_3 L_1 + \frac{1}{j\omega_3 C_1} \\ Z_{23} = R_2 + j\omega_3 L_2 + \frac{1}{j\omega_3 C_2} \end{cases} \quad (6)$$

Because the resonant frequencies of the transmitter and the receiver circuit are equal to the fundamental frequency of the driving source, the imaginary component of the impedance for the fundamental circuit is equal to zero, as shown in Equation (7).

$$\begin{cases} \omega_3 = 3\omega \\ j\omega L_1 + \frac{1}{j\omega C_1} = 0, j\omega L_2 + \frac{1}{j\omega C_2} = 0 \end{cases} \quad (7)$$

Substituting Equation (7) into Equation (6), the impedances for the fundamental and the third harmonics frequencies are represented as follows:

$$\begin{cases} Z_{11} = R_1 \\ Z_{21} = R_2 \\ Z_{13} = R_1 + 3j\omega L_1 + \frac{1}{3j\omega C_1} = R_1 + j\frac{8}{\omega C_1} \\ Z_{23} = R_2 + 3j\omega L_2 + \frac{1}{3j\omega C_2} = R_2 + j\frac{8}{\omega C_2} \end{cases} \quad (8)$$

$$\begin{cases} \dot{U}_{11} = \dot{I}_{11}(R_1 + \frac{\omega^2 M^2}{R_2}) \\ \dot{U}_{13} = \dot{I}_{13}(R_1 + j\frac{8}{3\omega C_1}) + \frac{9\omega^2 M^2}{(R_2 + j\frac{8}{\omega C_2})} \end{cases} \quad (9)$$

$$\omega^2 M^2 = R_2(\frac{\dot{U}_{11}}{\dot{I}_{11}} - R_1) \quad (10)$$

$$\dot{U}_{13} = \dot{I}_{13} \left[ R_1 + j\frac{8}{3\omega C_1} + \frac{9R_2(\frac{\dot{U}_{11}}{\dot{I}_{11}} - R_1)}{R_2 + j\frac{8}{\omega C_2}} \right] \quad (11)$$

Equation (9) is derived by substituting Equations (7) and (8) into Equation (5), and the upper equation of Equation (9) can be transformed to Equation (10). Both the transmitter and receiver are in the resonance state, whose frequency is the same as the fundamental component, so the right side of Equation (10) is a real number, and  $M^2$  is also a real number. Equation (11) is the result of substituting Equation (10) into the lower equation of Equation (9) and expressed as the linear equation form of  $R_2$ . From this, the upper equation of Equation (12) is obtained, namely  $R_2$ . The other way around,  $R_2$  of Equation (12) is substituted into Equation (10), and the expression of  $M$  is found, which may be positive and negative, but  $M$  cannot be negative theoretically, so the positive solution is taken, as follows, as the lower equation of Equation (12).

$$\begin{cases} R_2 = \frac{8j\dot{I}_{11}(3C_1\dot{I}_{13}R_1\omega - 3C_1\dot{U}_{13}\omega + 8j\dot{I}_{13})}{3C_2\omega(3C_1\dot{I}_{11}\dot{U}_{13}\omega - 27C_1\dot{I}_{13}\dot{U}_{11}\omega - 8j\dot{I}_{11}\dot{I}_{13} + 24C_1\dot{I}_{11}\dot{I}_{13}R_1\omega)} \\ M = \sqrt{\frac{(8\dot{U}_{11} - \dot{I}_{11}R_1)(3C_1\dot{I}_{13}R_1\omega - 3C_1\dot{U}_{13}\omega + 8j\dot{I}_{13})j}{3C_2\omega^3(3C_1\dot{I}_{11}\dot{U}_{13}\omega - 27C_1\dot{I}_{13}\dot{U}_{11}\omega - 8j\dot{I}_{11}\dot{I}_{13} + 24C_1\dot{I}_{11}\dot{I}_{13}R_1\omega)}} \end{cases} \quad (12)$$

The rising edge delay and the drop edge delay can be ignored due to the high speed characteristics of the switching element, and the duty cycle was 0.5, then the phase of the third harmonics voltage  $U_{13}$  was equal to one of the fundamental voltage  $U_{11}$ . Moreover, the LC circuits also resonated at the frequency of the fundamental wave, so the phase of fundamental current  $I_{11}$  was equal to the fundamental voltage  $U_{11}$ . This means that if the phase of  $U_{11}$  was considered as the reference point, the vector  $U_{11}$ ,  $U_{13}$ , and  $I_{11}$  of Equation (12) could be substituted with the scalars  $U_{11}$ ,  $U_{13}$ , and  $I_{11}$ , respectively. Therefore, there is only one vector component in Equation (12). Vector  $I_{13}$  is represented as complex and is shown as follows.

$$\dot{I}_{13} = |I_{13}| \cos(\alpha) + j|I_{13}| \sin(\alpha) \quad (13)$$

where  $|I_{13}|$  is the magnitude and  $\alpha$  is the phase of  $I_{13}$ . Equation (13) is substituted into Equation (12), and  $R_2$  and  $M$  are described as follows:

$$\begin{cases} R_2 = \frac{(R_{2\_nR} \times R_{2\_dR} - R_{2\_nI} \times R_{2\_dI}) + j(R_{2\_nR} \times R_{2\_dI} + R_{2\_nI} \times R_{2\_dR})}{R_{2\_dR}^2 \times R_{2\_dI}^2} \\ M = \sqrt{\frac{(XX\_nR \times R_{2\_dR} - XX\_nI \times R_{2\_dI}) + j(XX\_nR \times R_{2\_dI} + XX\_nI \times R_{2\_dR})}{\omega^2 (R_{2\_dR}^2 \times R_{2\_dI}^2)}} \end{cases} \quad (14)$$

where:

$$\begin{cases} R_{2\_dR} = 3C_2\omega(27C_1U_{11}\omega |I_{13}| \cos(\alpha) - 8I_{11} |I_{13}| \sin(\alpha) - 3C_1I_{11}U_{13}\omega - 24C_1I_{11}R_1\omega |I_{13}| \cos(\alpha)) \\ R_{2\_dI} = 3C_2\omega(8I_{11} |I_{13}| \cos(\alpha) + 27C_1U_{11}\omega |I_{13}| \sin(\alpha) - 24C_1I_{11}R_1\omega |I_{13}| \sin(\alpha)) \\ R_{2\_nR} = 8I_{11}(8 |I_{13}| \cos(\alpha) + 3C_1R_1\omega |I_{13}| \sin(\alpha)) \\ R_{2\_nI} = 8I_{11}(8 |I_{13}| \sin(\alpha) + 3C_1U_{13}\omega - 3C_1R_1\omega |I_{13}| \cos(\alpha)) \\ XX\_nR = 8(8 |I_{13}| \cos(\alpha) + 3C_1R_1\omega |I_{13}| \sin(\alpha))(U_{11} - I_{11}R_1) \\ XX\_nI = 8(8 |I_{13}| \sin(\alpha) + 3C_1U_{13}\omega - 3C_1R_1\omega |I_{13}| \cos(\alpha))(U_{11} - I_{11}R_1) \end{cases} \quad (15)$$

In theory, the load resistance and the mutual inductance will not be complex numbers, and for this reason, the real terms of Equation (14) are the load resistance and the mutual inductance expressions as follows.

$$\begin{cases} R_2 = \frac{(R_{2\_nR} \times R_{2\_dR} - R_{2\_nI} \times R_{2\_dI})}{R_{2\_dR}^2 \times R_{2\_dI}^2} \\ M = \sqrt{\frac{(XX\_nR \times R_{2\_dR} - XX\_nI \times R_{2\_dI})}{\omega^2 (R_{2\_dR}^2 \times R_{2\_dI}^2)}} \end{cases} \quad (16)$$

The imaginary parts of the load resistance  $R_2$  and the mutual inductance  $M$ , exploited according to Equation (14), are listed in Table 4 of Section 4. From this, it is noted that the imaginary parts were so small that they could be ignored, and this result coincided with the theory. Therefore, simplified Equation (16) may be used instead of Equation (14).

### 3. System Design

#### 3.1. S-S Topology MCR-WPT System

Figure 3 is the block diagram of the S-S topology MCR-WPT system.

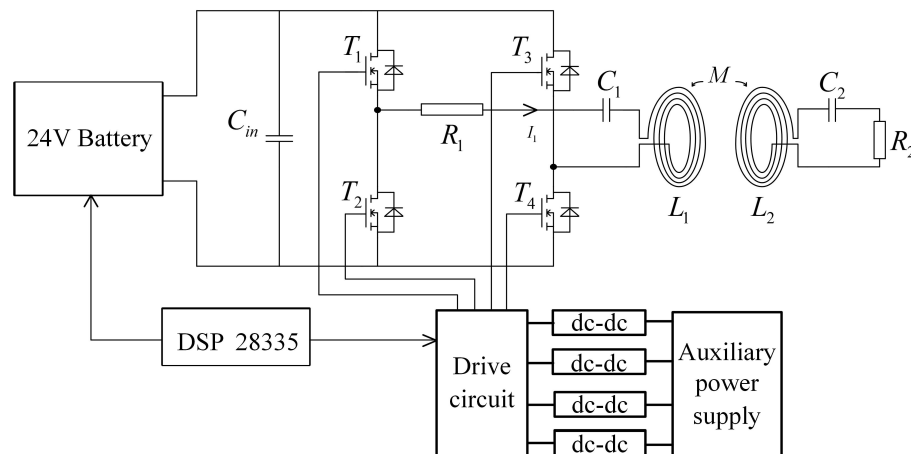


Figure 3. Block diagram of the S-S topology MCR-WPT system.

The high frequency power supply was composed of the high-frequency switching elements, the switching drive circuit. and the circuit with DSP28335 as the core for controlling the drive waveform. Even if the cost of the full-bridge four-switch inverter circuit is more expensive, it is commonly used in the MCR-WPT system, because of the diversity of driving modes and the lower

request for withstanding the voltage of switching elements. The resonance frequency of the system is directly concerned with the performance of the WPT system, and the higher the frequency of the system, the higher the frequency requirement of the switching elements. Earlier, SiC (Silicon Carbide) power MOSFET switching devices came onto the market, and they were widely used in Electric Vehicle (EV) battery chargers, renewable energy, the switched mode power supply, the high-voltage DC-DC converter, and so on. It has the merits of withstanding high voltage, a small switching-on resistance, and a very short switching time due to the low junction capacitance, and it has a high-speed reverse diode in itself, so it can meet the high frequency and high power requirement of the MRC-WPT system.

The experimental WPT system was designed with the C3M0065100K MOSFET of CREE Company [43] as the inverter switching elements. The DSP28335 module was the core for controlling the drive waveform, and a set of complementary symmetric pulses was generated to modulate the on-off state of the switching elements for the high-frequency inverter circuit. The drive circuit designed here was based on the SI8261BCD-C-ISR optical coupling isolation driver chip and the DC-DC converter MEJ2D1209SC, to amplify the DSP output signal and to isolate the signal from the power ground.

### 3.2. Planar Circular Spiral Coil

The structure of the planar spiral coil is simple, and the thickness of such a coil is thin. In addition to these merits, the magnetic field generated by such a coil current is relatively balanced and therefore less sensitive to the small attitude changes; for this reason, it is commonly used for the MCR-WPT system. The coil structure used in the experiment was a planar circular spiral structure, and its geometric parameters are as follows: The diameter of the inner loop was 140 mm, and the diameter of the outer loop was 300 mm. The interval distance between the adjacent loops was constant, equal to 10 mm, and the number of turns was eight. The diameter of the copper winding wire was 2.5 mm. In order to facilitate winding the coil, the plastic base plate for fixing of the copper wire was printed by a 3D printer. A concave, same as the coil, shape was engraved on this plate, and then, the copper wire was clamped onto the base plate.

Figure 4 is the base plate and the photograph of the transmitter and receiver coils (the two coils are the same). The self-inductance of the coil in Figure 4 can be calculated using Equations (5) and (6) of [44], and the value  $L_1 = L_2 = 17.462 \mu\text{H}$ .

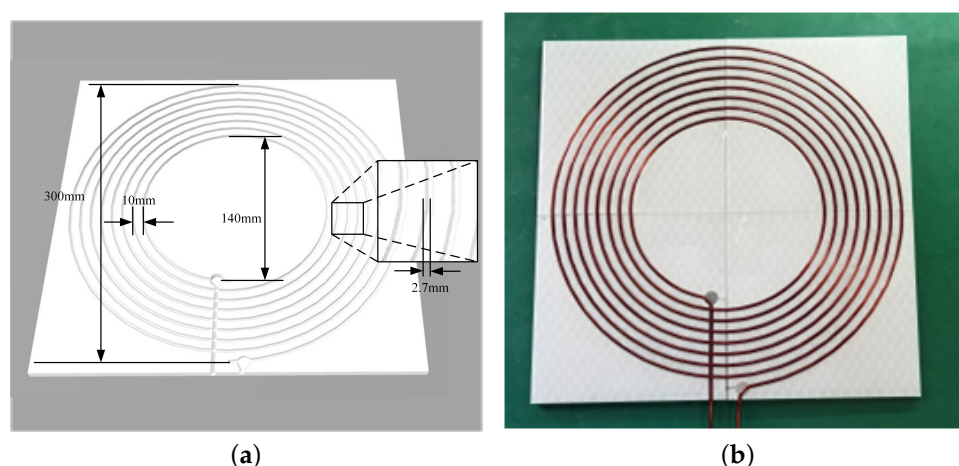


**Figure 4.** Planar circular spiral coil: (a) Rendering graph of the base plate; (b) photograph of the coil.

## 4. Simulation Study

The switching element used here was not in the normal element database; hence, it cannot be found in the SPICE software. The file where the parameters of the switch element are described would be imported through the database addition function of the SPICE software. The SPICE database

file of the switching element is provided by the provider of the switching element, and it can be used for simulating the circuit that contains these switching elements. There are three types in the power switching MOSFETs C3M0065090 series, and C3M0065090D with three pins was used for the convenience of the design and installation of the large heat sinks. Firstly, we downloaded C3M0065090D.lib to the simulation computer from <http://go.wolfspeed.com/all-models>. Secondly, we extracted the C3M0065090D.OLB file from this file, imported it into the simulation folder, and added the simulation database.

Figure 5 is the simulation schematic diagram of the system. In order to simplify the simulation process and shorten the simulation time, the four pulse wave sources were used to drive the gates of the four power switching elements. The phase of each pulse source was in phase with the phase of this diagonal one, and the phase difference between the upper and lower was 180 degrees.

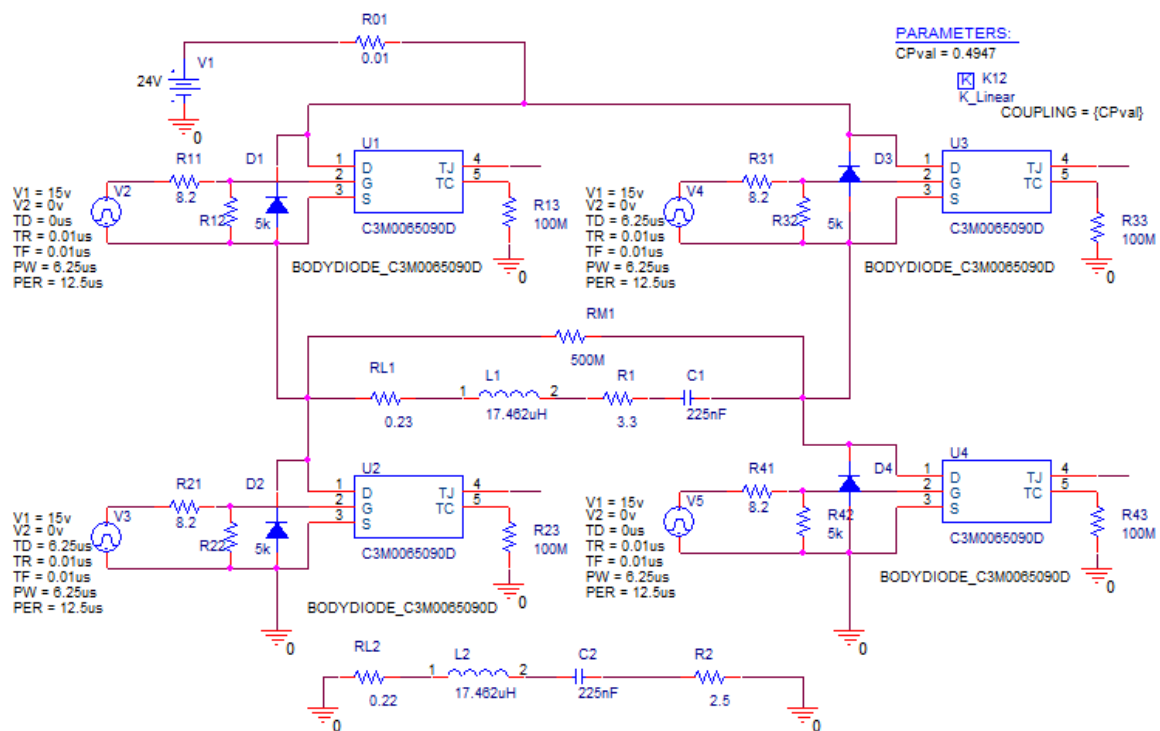


Figure 5. Simulation schematic diagram.

$R_{L1}$  and  $R_{L2}$  are the resistances of the transmitter and receiver coil, respectively, based on the values measured by the network analyzer, and listed in Table 1.  $R_1$  and  $R_2$  are the protection and the load resistance, respectively.  $L_1$ ,  $C_1$ ,  $L_2$ , and  $C_2$  are the self-inductance and compensated capacitance of the transmitter and receiver, respectively. PARAMETERS is used to describe the variable.  $K_{12}$  is the coupling coefficient between  $L_1$  and  $L_2$  and is defined as variable by PARAMETERS.  $U_1$ ,  $U_2$ ,  $U_3$ , and  $U_4$  are switching elements, and  $D_1$ ,  $D_2$ ,  $D_3$ , and  $D_4$  are the reverse diodes of the switching elements themselves.  $R_{M1}$  is a high-value resistor, which is in fact meaningless for the system operation, but is intentionally added to measure the output voltage and is never in the actual experimental circuit. The resonant frequency calculated according to the LC parameter of Table 1 was 80.3 kHz.  $V_2$ ,  $V_3$ ,  $V_4$ , and  $V_5$  are the signal source for the four MOSFET gates, and the parameters are shown in Table 2.

**Table 1.** Element parameters of the simulation schematic diagram.

Symbol	Name	Value	Unit
$V_1$	DC battery	24	V
$L_1$	Primary coil inductance	17.462	$\mu\text{H}$
$L_2$	Secondary coil inductance	17.462	$\mu\text{H}$
$C_1$	Primary compensation capacitance	225	nF
$C_2$	Secondary compensation capacitance	225	nF
$R_1$	Primary serial resistor	3.3	$\Omega$
$R_2$	Secondary serial resistor	1, 2.5, 3.3, 5	$\Omega$
$R_{L1}$	Primary parasitic resistor	0.23	$\Omega$
$R_{L2}$	Secondary parasitic resistor	0.22	$\Omega$

**Table 2.** Parameters for driving the MOSFET gates.

Symbol	$V_1$	$V_2$	$T_D$	$T_R$	$T_F$	PW	PER
Name	High level Voltage	Low level Voltage	Time of delay	Time of rising edge	Time of falling edge	Pulse width	
Value	15	0	0	0.01	0.01	6.23	12.45
Unit	V	V	$\mu\text{s}$	$\mu\text{s}$	$\mu\text{s}$	$\mu\text{s}$	$\mu\text{s}$

There is no mutual inductance parameter in the SPICE software, so the mutual inductance parameter cannot be used directly in the simulation. Fortunately, the coupling parameter was in SPICE software, while it can be represented with the mutual inductance and the self-inductance of two coils; thus, the two-coil topology circuit can be simulated by it.

According to Equation (4) of [45] and Equation (7) of [44], the mutual inductance can be calculated for the distance variation between the two coils, which has the structure as shown in Figure 4. Then, the coupling coefficients with respect to the distance can be calculated by using these mutual inductances and self-inductances. The mutual inductances and the coupling coefficients calculated are represented in Table 3.

**Table 3.** Mutual inductance and coupling coefficient according to the distance variation.

Distance (cm)	2	3	4	5	6	7
Mutual inductance ( $\mu\text{H}$ )	11.92	10.11	8.64	7.43	6.42	5.57
Coupling Coefficient	0.6826	0.5790	0.4947	0.4253	0.3676	0.3193

In the simulation schematic diagram, CPval assigned to the PARAMETERS: represents the coupling coefficient between the transmitter ( $L_1$ ) and receiver coil ( $L_2$ ), and this is shown in the coupling coefficient row of Table 3.

Figures 6 and 7 are the simulation results in the case of  $R_2 = 2.5 \Omega$ ,  $d = 4$  cm. Figure 6a,b is the voltage across the gate and source of the switching elements  $U_1$  and  $U_2$ , where the two rectangle waveforms are complementary. Figure 6c,d is the output voltage and current waveform of the high-frequency inverter. The voltage waveform was almost similar to a rectangle wave, and the current waveform was similar to a sinusoidal wave. Figure 6e is the result of the FFT spectrogram analysis of Figure 6c, while Figure 6f is that of Figure 6d. As shown in Figure 6, not a very much of the harmonic components was contained in the output voltage waveform, while the output current was not so large.

Figure 7a,b is the examples in which the FFT analysis results for the output voltage and output current are expressed as the list form. In Figure 7, HARMONIC NO is the harmonic order, FOURIER COMPONENT is the corresponding harmonic amplitude, and PHASE is depicted as the phase of the corresponding harmonic where the unit is the degree. From Figure 7, it can be known that the odd harmonic components had a relatively large amplitude, and the phase of the fundamental voltage was close to zero (0.487); the phase of the third harmonic voltage was also similar to zero (1.9); and the

phase of the fundamental current was close to 180 degrees (179.5). Based on the above, the fundamental output voltage, the third harmonic voltage, and the fundamental output current can be considered as scalars. At the same way, the FFT analysis for the output voltage and current was repeated in the case with the different distances and different loads. The phases of the fundamental and third harmonic components were similar to those mentioned above. The magnitudes for the fundamental and the third harmonics components of the output voltage and current were found at the same time. The result obtained by substituting the magnitude and the phase values into Equation (16) is shown in Figure 8.

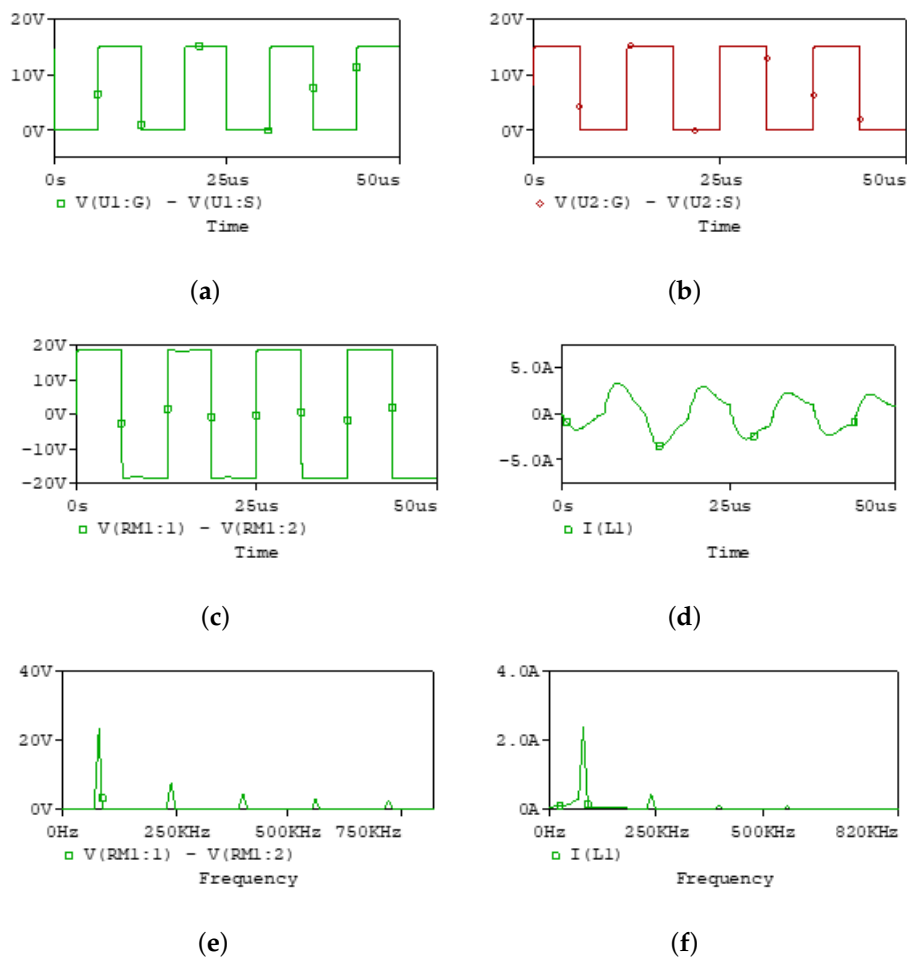


**Figure 6.** Simulation result. (a) Waveform at the gate of  $U_1$ ; (b) waveform at the gate of  $U_2$ ; (c) waveform of the output voltage; (d) waveform of the output current; (e) FFT spectrum analysis of (c); (f) FFT spectrum analysis of (d).

FOURIER COMPONENTS OF TRANSIENT RESPONSE I(R\_R1)

DC COMPONENT = -5.595592E-03

HARMONIC NO	FREQUENCY (HZ)	FOURIER COMPONENT	NORMALIZED COMPONENT	PHASE (DEG)	NORMALIZED PHASE (DEG)
1	8.030E+04	2.265E+00	1.000E+00	1.795E+02	0.000E+00
2	1.606E+05	1.391E-02	6.142E-03	-1.433E+02	-5.024E+02
3	2.409E+05	4.661E-01	2.058E-01	1.054E+02	-4.333E+02
4	3.212E+05	6.439E-03	2.842E-03	-1.693E+02	-8.875E+02
5	4.015E+05	1.501E-01	6.624E-02	9.846E+01	-7.993E+02
6	4.818E+05	4.108E-03	1.813E-03	-1.769E+02	-1.254E+03
7	5.621E+05	7.438E-02	3.283E-02	9.630E+01	-1.161E+03

TOTAL HARMONIC DISTORTION = 2.187443E+01 PERCENT

(a)

FOURIER COMPONENTS OF TRANSIENT RESPONSE U(R\_RM1)

DC COMPONENT = 1.388612E-01

HARMONIC NO	FREQUENCY (HZ)	FOURIER COMPONENT	NORMALIZED COMPONENT	PHASE (DEG)	NORMALIZED PHASE (DEG)
1	8.030E+04	2.358E+01	1.000E+00	4.872E-01	0.000E+00
2	1.606E+05	2.781E-01	1.179E-02	9.224E+01	9.126E+01
3	2.409E+05	7.924E+00	3.361E-01	1.902E+00	4.404E-01
4	3.212E+05	2.793E-01	1.184E-02	9.411E+01	9.216E+01
5	4.015E+05	4.753E+00	2.016E-01	2.756E+00	3.204E-01
6	4.818E+05	2.799E-01	1.187E-02	9.604E+01	9.311E+01
7	5.621E+05	3.389E+00	1.437E-01	3.731E+00	3.209E-01

TOTAL HARMONIC DISTORTION = 4.179162E+01 PERCENT

(b)

Figure 7. Analysis result represented as the list form. (a) List of the FFT analysis result for the output voltage; (b) list of the FFT analysis result for the output current.

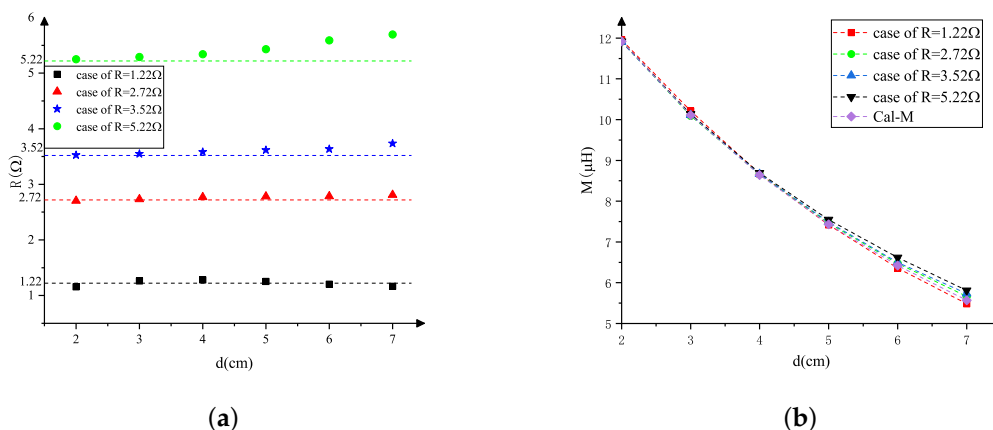


Figure 8. Calculation result of load resistance and mutual inductance. (a) Load resistance; (b) mutual inductance.

The values of 1, 2.5, 3.3, and 5 Ω were used in the simulation as the load resistances, and the stray resistance of the receiver coil itself, which was not ignored, was 0.22 Ω; it was also taken into account in the simulation circuit. Therefore, it is reasonable that the calculated resistances were compared with

1.22, 2.72, 3.52, and 5.22  $\Omega$ . From Figure 8, it is not difficult to see that the load resistances and the mutual inductances that were estimated from Equation (16) were near the actual values defined in the simulation circuit. This implied that the larger the load resistance was, the larger the error of the load resistance estimated, and the farther the distance was, the greater the error of the load resistance and the mutual inductance estimated.

Table 4 is the imaginary parts of the load resistance  $R_2$  and the mutual inductance  $M$  solved according to Equation (14). As shown in Table 4, the imaginary parts were so small that they could be ignored, and the simplified Equation (16) was used to calculate  $R_2$  and  $M$  instead of Equation (14).

**Table 4.** Imaginary parts of  $R_2$  and  $M$  in the simulation.

Distance (cm)	$M$ ( $\mu\text{H}$ )	$R_2 = 1.22 \Omega$		$R_2 = 2.72 \Omega$		$R_2 = 3.52 \Omega$		$R_2 = 5.22 \Omega$	
		Im_R	Im_M	Im_R	Im_M	Im_R	Im_M	Im_R	Im_M
2	11.92	0.0398	0.2052	0.0313	0.069	0.0223	0.0376	0.0257	0.0292
3	10.11	0.0838	0.3389	0.0582	0.1075	0.0621	0.0885	0.085	0.0814
4	8.64	0.0875	0.2955	0.1144	0.1789	0.1319	0.1595	0.1802	0.1466
5	7.43	0.1016	0.3002	0.1918	0.257	0.2495	0.2582	0.3804	0.2639
6	6.42	0.1281	0.3369	0.2993	0.3469	0.3708	0.3306	0.6122	0.3612
7	5.57	0.2021	0.4715	0.5013	0.5014	0.6533	0.4981	0.883	0.4476

## 5. Experimental Verification

Figure 9 is the photo of the experimental setup, which was similar to the general MCR-WPT system. According to the block diagram of the S-S topology MCR-WPT system of Section 3, it was composed of a DC battery, auxiliary power supply, DSP28335 module, inverter module, which was focused on the SiC power switching element, protection resistance, transmitter and receiver coils, which were the same size, and transmitter and receiver compensation capacitances and load resistances. The parameters of the resistances, inductances, and capacitances used in this experimental setup are shown in Table 5. All parameters in Table 5 were measured by the network analyzer Keysight E5061B.

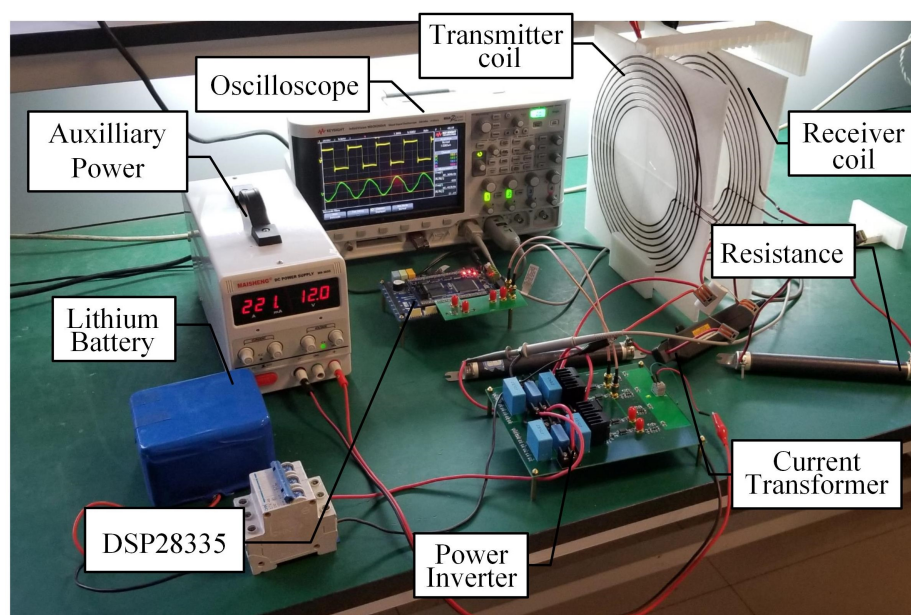


**Figure 9.** Experimental setup.

**Table 5.** Element parameters of the simulation schematic diagram.

Symbol	Name	Value	Unit
$V_1$	DC battery	24	V
$L_1$	Primary coil inductance	17.021	$\mu\text{H}$
$L_2$	Secondary coil inductance	16.996	$\mu\text{H}$
$C_1$	Primary compensation capacitance	224.96	nF
$C_2$	Secondary compensation capacitance	225.12	nF
$R_1$	Primary serial resistor	2.87	$\Omega$
$R_2$	Secondary serial resistor	0.93, 2.04, 3.20, 4.53	$\Omega$
$R_{L1}$	Primary parasitic resistor	0.2297	$\Omega$
$R_{L1}$	Secondary parasitic resistor	0.2165	$\Omega$

In fact, the resonant frequency calculated with the parameters of Table 5 was about 81.3 kHz, but the resonance frequency measured by the network analyzer was 80.3 kHz because of the influence of the connection inductance of the coil and the stray inductance of the resistor. It happened to be the same as the frequency in the simulation of Section 4. The output voltage of the inverter was measured by the oscilloscope probe, and the Current Transformer KEYSIGHT 1147B was used to measure the output current of the transmitter, while the current was converted into the voltage. The phase delay of the current transformer could be considered as zero. The measured voltage and current were input to the Oscilloscope KEYSIGHT Infiniivision MSOX2024A, in which the data for the waveforms could be displayed and saved. According to the direction of the current clamp and the oscilloscope probe, the phase of the measured voltage and current was different; in other words, the phase difference was equal to either zero or 180 degrees.

When the load resistance was 0.93  $\Omega$ , the distance was adjusted from 2–7 cm, while the data of the output voltage and current were measured and saved. This process was repeated for 2.04, 3.20, and 4.53  $\Omega$  resistances. The MATLAB software was utilized to perform FFT analysis for the experiment data measured, where the fundamental frequency was 80.3 kHz. Figures 10 and 11 are the analysis results when the distance was 4 cm and the load resistance was 2.04  $\Omega$ . Figure 10 is the FFT analysis result of the output voltage, and Figure 11 is that for the output current. The upper curve of the graph is the output waveform with respect to time, and the lower table is the analysis result with respect to the frequency.

Through the above process, the amplitude and the phase of the fundamental and third harmonic components were obtained with respect to the load resistance and the distance change. Substituting these amplitude and the phases into Equation (16), the result is shown in Figure 12.

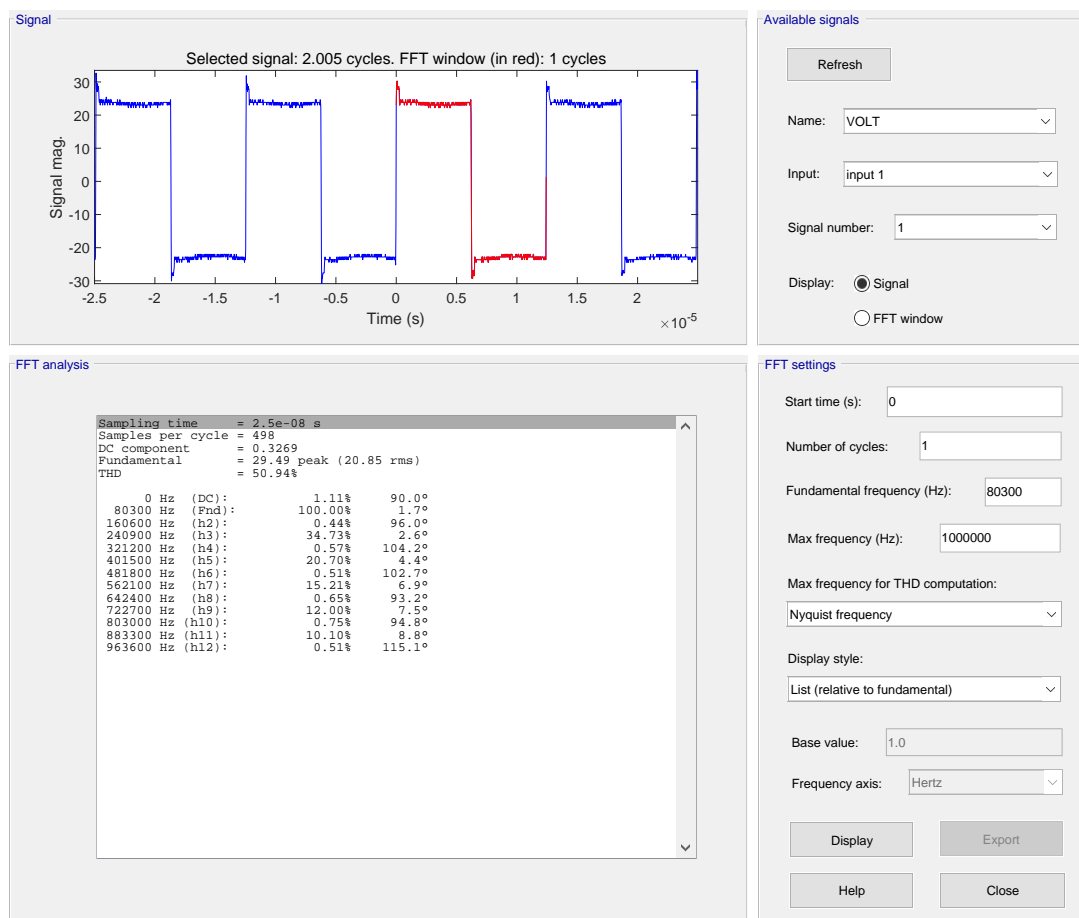


**Figure 10.** FFT analysis result for output voltage measured in the experimental setup.

Figure 12a is the experimental result for the resistances, and Figure 12b is the experimental results for the mutual inductances. In Figure 12a, the resistance values were nearer to the actual value at 2–6 cm, but became smaller at 7 cm. In Figure 12b, the trend of the mutual inductance was very similar to the calculated value, but the measured values were smaller than the calculated value. In Figure 12b, the real-Mcurve is the calculated value, and the oldExp-M curve is the experimental result implemented in [21]. The deviation between the actual and the experimental values was mainly concerned with the coils made by hand and the misalignment between the coils during the experiment. Strictly speaking, as the frequencies of the transmitter and the receiver were not the same as the frequency of the driving source, a small deviation of the amplitude and the phase happened and affected the accuracy of the estimated value. The resistance of the coil was related to the frequency: the higher the frequency, the higher the AC (Alternative Current) resistance of the coil. Moreover, the temperature change characteristics of the resistance and the switching element were not considered during the experiment.

Although the experimental results were slightly different from the simulation and the actual values in the case of when the transfer distance was long and the load resistance was large, the estimated value was very close to the actual value in the case of when the transfer distance was not long and the load resistance was not large, so this method can be recommended for high-power and short-distance WPT applications such as furnaces and kitchen appliances.

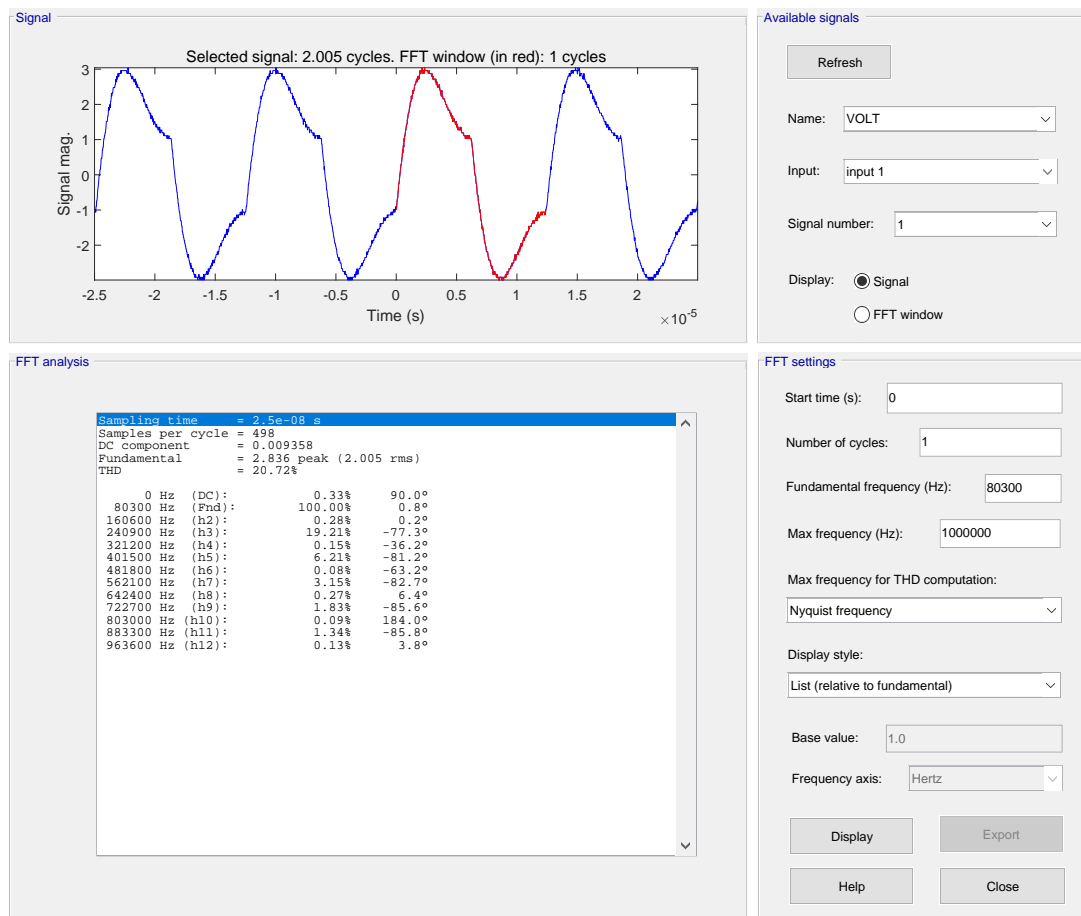


Figure 11. FFT analysis result for the output current measured in the experimental setup.

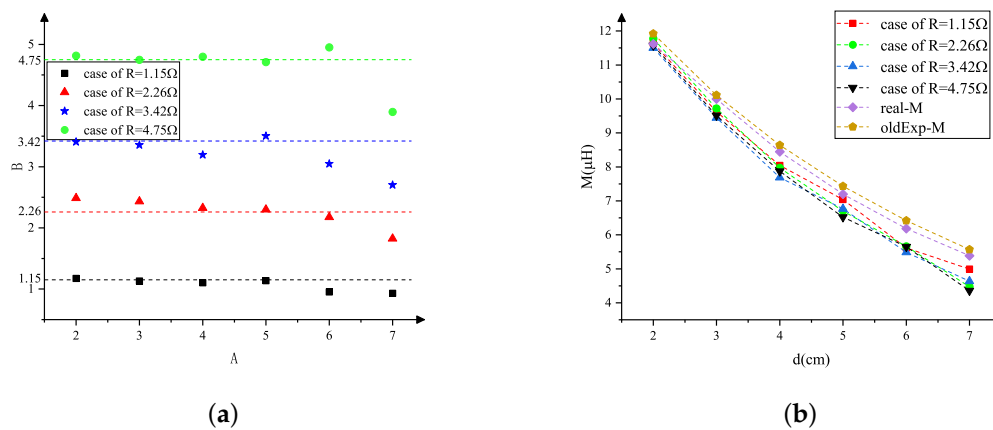


Figure 12. Experimental results for load resistances and mutual inductances. (a) Load resistance; (b) mutual inductance.

## 6. Conclusions

A method for simultaneously estimating the mutual inductance and the load resistance of the system without the communication function was represented in this paper, and this method can be applied to the general ferrite-free coil WPT system. In order to reduce on-off losses of the switching elements, most WPT systems are driven by rectangle signals. Therefore, the harmonic components, as well as the fundamental component are parasitic in the system, and they are incidentally used to

calculate the mutual inductance and the load resistance. In the paper, the rectangle-driven circuit was decomposed into several different component circuits according to the odd order harmonic frequencies, and then, Kirchhoff's voltage law was applied to these circuits to obtain the mutual inductance and the load resistance. In order to verify the effectiveness of the method, the simulation software SPICE was used. Furthermore, the experimental circuit with the SiC power MOSFET as the switching element was designed, and then, the effectiveness of the method was proven on this circuit. It did not need to sweep the frequency, and the time for sweeping may be shortened; moreover, it was not necessary to add some accessories and operations in order to estimate the mutual inductance and the load resistance simultaneously. During the simulation and the experiment process, only the distance change was considered here, but in fact, not a geometric parameter, but a mutual inductance was used in the calculation process, so it can be utilized in other cases such as lateral offset. Besides WPT systems, it was also used to estimate the mutual inductance of the other system.

**Author Contributions:** All authors have cooperated in the preparation of this work. Conceptualization, S.W., J.T., and D.Y.; methodology, S.W.; software, J.T.; validation, Z.C. and J.K.; formal analysis, J.T.; writing, original draft preparation, S.W.; writing, review and editing, S.W. and J.T.; visualization, Z.C. and J.K.; project administration, D.Y.

**Funding:** This research was funded by National Natural Science Foundation of China, No. 61703081, the Natural Science Foundation of Liaoning Province, No. 20170520113, and the State Key Laboratory of Alternate Electrical Power System with Renewable Energy Sources, No. LAPS19005.

**Acknowledgments:** The authors gratefully acknowledge financial support from the National Natural Science Foundation of China, No. 61703081, the Natural Science Foundation of Liaoning Province, No. 20170520113, and the State Key Laboratory of Alternate Electrical Power System with Renewable Energy Sources, No. LAPS19005. We appreciate our colleagues' support and the help from the College of Information Science and Engineering at Northeastern University.

**Conflicts of Interest:** The authors declare no conflict of interest.

## References

1. Kang, S.H.; Choi, J.H.; Jung, C.W. Magnetic resonance wireless power transfer using three-coil system with single planar receiver for laptop applications. *IEEE Trans. Consum. Electron.* **2015**, *61*, 160–166.
2. Olvitz, L.; Vinko, D.; Švedek, T. Wireless power transfer for mobile phone charging device. *MEET-Microelectron. Electron. Technol.* **2012**, *98*, 141–145.
3. Moon, S.C.; Moon, G.W. Wireless power transfer system with an asymmetric 4-coil resonator for electric vehicle battery chargers. In Proceedings of the 2015 IEEE Applied Power Electronics Conference and Exposition (APEC), Charlotte, NC, USA, 15–19 March 2015; pp. 1650–1657.
4. Kusaka, K.; Itoh, J. Input impedance matched AC-DC converter in wireless power transfer for EV charger. In Proceedings of the 2012 15th International Conference on Electrical Machines and Systems (ICEMS), Sapporo, Japan, 21–24 October 2012; pp. 1–6.
5. Mutashar, S.; Hannan, M.; Samad, S.; Hussain, A. Analysis and Optimization of Spiral Circular Inductive Coupling Link for Bio-Implanted Applications on Air and within Human Tissue. *Sensors* **2014**, *14*, 11522–11541. [[CrossRef](#)] [[PubMed](#)]
6. Tang, S.C.; Lun, T.L.T.; Guo, Z.; Kwok, K.W.; McDannold, N.J. Intermediate Range Wireless Power Transfer with Segmented Coil Transmitters for Implantable Heart Pumps. *IEEE Trans. Power Electron.* **2017**, *32*, 3844–3857. [[CrossRef](#)]
7. Ko, W.H.; Liang, S.P.; Fung, C.D. Design of radio-frequency powered coils for implant instruments. *Med. Biol. Eng. Comput.* **1977**, *15*, 634–640. [[CrossRef](#)] [[PubMed](#)]
8. Kim, J.; Son, H.C.; Kim, D.H.; Park, Y.J. Optimal design of a wireless power transfer system with multiple self-resonators for an LED TV. *IEEE Trans. Consum. Electron.* **2012**, *58*, 775–780. [[CrossRef](#)]
9. Bu, Y.; Mukhopadhyay, S.C. Equalization Method of the Wireless Power Transfer in an Electronic Shelf Label Power Supply System. *IEEE Trans. Magn.* **2017**, *53*, 1–5.
10. Miyamura, K.; Miyaji, Y.; Ohmura, R. Feasibility study on wireless power transfer for wearable devices. In Proceedings of the 2017 ACM International Symposium on Wearable Computers (ISWC'17), Maui, HI, USA, 11–15 September 2017; pp. 166–167.

11. Liao, W.; Shi, J.; Wang, J. Electromagnetic interference of wireless power transfer system on wearable electrocardiogram. *IET Microw. Antennas Propag.* **2017**, *11*, 330–335. [[CrossRef](#)]
12. Nguyen, C.; Kota, P.; Nguyen, M.; Dubey, S.; Rao, S.; Mays, J.; Chiao, J.C. Wireless Power Transfer for Autonomous Wearable Neurotransmitter Sensors. *Sensors* **2015**, *15*, 24553–24572. [[CrossRef](#)]
13. Ryu, H.G.; Har, D. Wireless Power Transfer for High-precision Position Detection of Railroad Vehicles. In Proceedings of the 2015 IEEE Power, Communication and Information Technology Conference (PCITC), Bhubaneswar, India, 15–17 October 2015; pp. 1–4.
14. Villa, J.L.; Sanz, J.F.; Perié, J.M.; Acerete, R.; Bludszuweit, H. Wireless power supply for mobile aluminum furnaces. In Proceedings of the 2018 International Symposium on Industrial Electronics (INDEL), Banja Luka, Bosnia and Herzegovina, 1–3 November 2018; pp. 1–6.
15. Wang, Z.; Li, Y.; Sun, Y.; Tang, C.; Lv, X. Load Detection Model of Voltage-Fed Inductive Power Transfer System. *IEEE Trans. Power Electron.* **2013**, *28*, 5233–5243. [[CrossRef](#)]
16. Itraj, M.; Ettes, W. Topology Study for an Inductive Power Transmitter for Cordless Kitchen Appliances. In Proceedings of the 2018 IEEE PELS Workshop on Emerging Technologies: Wireless Power Transfer (Wow), Montréal, QC, Canada, 3–7 June 2018; pp. 1–8.
17. Nataraj, C.; Khan, S.; Eniola, F.F.; Selvaperumal, S.K. Design of simple DC-to-DC Wireless Power Transfer via inductive coupling. In Proceedings of the 2017 Third International Conference on Advances in Electrical, Electronics, Information, Communication and Bio-Informatics (AEEICB), Chennai, India, 27–28 February 2017; pp. 1–6.
18. Matias, R.; Cunha, B.; Martins, R.P. Modeling inductive coupling for Wireless Power Transfer to integrated circuits. In Proceedings of the 2013 IEEE Wireless Power Transfer (WPT), Perugia, Italy, 15–16 May 2013; pp. 198–201.
19. Zaman, H.U.; Islam, T.; Hasan, K.S.; Antora, R.K. Mobile phone to mobile phone wireless power transfer. In Proceedings of the 2015 International Conference on Advances in Electrical Engineering (ICAEE), Dhaka, Bangladesh, 17–19 December 2015; pp. 206–209.
20. Hong, H.; Yang, D.; Won, S. The Analysis for Selecting Compensating Capacitances of Two-Coil Resonant Wireless Power Transfer System. In Proceedings of the 2017 IEEE International Conference on Energy Internet (ICEI), Beijing, China, 17–21 April 2017; pp. 220–225.
21. Won, S.; Yang, D.; Tian, J.; Cheng, Z.; Jon, S. A mutual inductance measurement method for the wireless power transfer system. In Proceedings of the 2019 4th Asia Conference on Power and Electrical Engineering (ACPEE 2019), Hangzhou, China, 28–31 March 2019; pp. 1–8, accepted.
22. Fnato, H.; Chiku, Y.; Harakawa, K. Wireless power distribution with capacitive coupling excited by switched mode active negative capacitor. In Proceedings of the 2010 International Conference on Electrical Machines and Systems, Incheon, Korea, 10–13 October 2010; pp. 1–6.
23. Hagen, S.; Knippel, R.; Dai, J.; Ludois, D.C. Capacitive coupling through a hydrodynamic journal bearing to power rotating electrical loads without contact. In Proceedings of the 2015 IEEE Wireless Power Transfer Conference (WPTC), Boulder, CO, USA, 13–15 May 2015; pp. 1–4.
24. Li, X.; Luk, K.M.; Duan, B. Multiobjective Optimal Antenna Synthesis for Microwave Wireless Power Transmission. *IEEE Trans. Antennas Propag.* **2019**, *67*, 2739–2744. [[CrossRef](#)]
25. Rajabi, M.; Pan, N.; Claessens, S.; Pollin, S.; Schreurs, D. Modulation Techniques for Simultaneous Wireless Information and Power Transfer with an Integrated Rectifier-Receiver. *IEEE Trans. Microw. Theory Technol.* **2018**, *66*, 2373–2385. [[CrossRef](#)]
26. Huang, Y.; Clerckx, B. Waveform Design for Wireless Power Transfer with Limited Feedback. *IEEE Trans. Wirel. Commun.* **2017**, *17*, 415–429. [[CrossRef](#)]
27. Leung, H.F.; Hu, A.P. Theoretical modeling and analysis of a wireless Ultrasonic Power Transfer system. In Proceedings of the 2015 IEEE PELS Workshop on Emerging Technologies: Wireless Power (WoW), Daejeon, Korea, 5–6 June 2015; pp. 1–6.
28. Zhang, Q.; Fang, W.; Liu, Q.; Wu, J.; Xia, P.; Yang, L. Distributed Laser Charging: A Wireless Power Transfer Approach. *IEEE Internet Things J.* **2018**, *5*, 3853–3864. [[CrossRef](#)]
29. Sample, P.; Meyer, D.A.; Smith, J.R. Analysis experimental results, and range adaption of magnetically coupled resonators for wireless power transfer. *IEEE Trans. Ind. Electron.* **2011**, *58*, 544–554. [[CrossRef](#)]

30. Yang, D.; Won, S.; Hong, H. Design of Range Adaptive Wireless Power Transfer System Using Non-coaxial Coils. In Proceedings of the 2017 2nd Asia Conference on Power and Electrical Engineering (ACPEE 2017), Shanghai, China, 24–26 March 2017; pp. 1–8.
31. Zhong, W.; Hui, S.Y.R. Maximum Energy Efficiency Operation of Series-Series Resonant Wireless Power Transfer Systems Using On-Off Keying Modulation. *IEEE Trans. Power Electron.* **2017**, *33*, 3595–3603. [[CrossRef](#)]
32. Zhu, G.; Mai, S.; Zhang, C.; Wang, Z. Distance and load insensitive inductive powering for implantable medical devices through wireless communication. In Proceedings of the 2017 IEEE Wireless Power Transfer Conference (WPTC), Taipei, Taiwan, 10–12 May 2017; pp. 1–3.
33. Fu, M.; Yin, H.; Liu, M.; Wang, Y.; Ma, C. A 6.78 MHz Multiple-Receiver Wireless Power Transfer System With Constant Output Voltage and Optimum Efficiency. *IEEE Trans. Power Electron.* **2018**, *33*, 5330–5340. [[CrossRef](#)]
34. Liu, F.; Chen, K.; Zhao, Z.; Li, K.; Yuan, L. Transmitter-Side Control of Both the CC and CV Modes for the Wireless EV Charging System with the Weak Communication. *IEEE J. Emerg. Sel. Top. Power Electron.* **2018**, *6*, 955–965. [[CrossRef](#)]
35. Li, X.; Wang, H.; Dai, X. A Power and Data Decoupled Transmission Method for Wireless Power Transfer Systems via a Shared Inductive Link. *Energies* **2018**, *11*, 2161. [[CrossRef](#)]
36. Liu, F.; Zhao, Z.; Zhang, Y.; Chen, K.; He, F.; Yuan, L. A selection method of mutual inductance identification models based on sensitivity analysis for wireless electric vehicles charging. In Proceedings of the IEEE Energy Conversion Congress and Exposition (ECCE), Milwaukee, WI, USA, 18–22 September 2016; pp. 1–6.
37. Jiwariyavej, V.; Imura, T.; Hori, Y. Coupling Coefficients Estimation of Wireless Power Transfer System via Magnetic Resonance Coupling Using Information from Either Side of the System. *IEEE J. Emerg. Sel. Top. Power Electron.* **2015**, *3*, 191–200. [[CrossRef](#)]
38. Yin, J.; Lin, D.; Parisini, T.; Hui, S.R. Front End Monitoring of the Mutual Inductance and Load Resistance in a Series-Series Compensated Wireless Power Transfer System. *IEEE Trans. Power Electron.* **2015**, *31*, 7339–7352. [[CrossRef](#)]
39. Su, Y.G.; Zhang, H.Y.; Wang, Z.H.; Hu, A.P.; Chen, L.; Sun, Y. Steady-State Load Identification Method of Inductive Power Transfer System Based on Switching Capacitors. *IEEE Trans. Power Electron.* **2015**, *30*, 6349–6355. [[CrossRef](#)]
40. Nutwong, S.; Sangswang, A.; Naetiladdanon, S.; Mujjalinvimut, E. A Novel Output Power Control of Wireless Powering Kitchen Appliance System with Free-Positioning Feature. *Energies* **2018**, *11*, 1671. [[CrossRef](#)]
41. Su, Y.G.; Chen, L.; Wu, X.Y.; Hu, A.P.; Tang, C.S.; Dai, X. Load and Mutual Inductance Identification from the Primary Side of Inductive Power Transfer System with Parallel-Tuned Secondary Power Pickup. *IEEE Trans. Power Electron.* **2018**, *33*, 9952–9962. [[CrossRef](#)]
42. Zeng, H.; Yang, S.; Peng, F.Z. Design Consideration and Comparison of Wireless Power Transfer via Harmonic Current for PHEV and EV Wireless Charging. *IEEE Trans. Power Electron.* **2017**, *32*, 5943–5952. [[CrossRef](#)]
43. CREE. C3M0065090D Silicon Carbide Power MOSFET Datasheet. Available online: <https://www.alldatasheet.com/datasheet-pdf/pdf/798446/CREE/C3M0065090D.html> (accessed on 5 August 2018).
44. Zierhofer, C.M.; Hochmair, E.S. Geometric approach for coupling enhancement of magnetically coupled coils. *IEEE Trans. Biomed. Eng.* **1996**, *43*, 708–714. [[CrossRef](#)] [[PubMed](#)]
45. Grover, F.W. The Calculation of the Mutual Inductance of Circular Filaments in Any Desired Positions. *Proc. IRE* **1944**, *32*, 620–629. [[CrossRef](#)]

